

Probing quantum causality with geometric asymmetry in spatial-temporal correlations

Yu MENG^{1,2}, Zheng-Hao LIU^{1,2}, Zhikuan ZHAO^{3*}, Peng YIN^{1,2}, Yi-Tao WANG^{1,2,6}, Wei LIU^{1,2,6}, Zhi-Peng LI^{1,2,6}, Yuan-Ze YANG^{1,2}, Zhao-An WANG^{1,2}, Jin-Shi XU^{1,2,6}, Shang YU^{4,1,5*}, Jian-Shun TANG^{1,2,6*}, Chuan-Feng LI^{1,2,6*} & Guang-Can GUO^{1,2,6}

¹CAS Key Laboratory of Quantum Information,

University of Science and Technology of China, Hefei 230026, China;

²CAS Center for Excellence in Quantum Information and Quantum Physics,
University of Science and Technology of China, Hefei 230026, China;

³Department of Computer Science, Eidgenössische Technische Hochschule Zürich, Zürich 8092, Switzerland;

⁴Department of Physics, Imperial College London, London SW7 2AZ, UK;

⁵Research Center for Quantum Sensing, Zhejiang Lab, Hangzhou 310000, China;

⁶Hefei National Laboratory, Hefei 230088, China

Received 8 January 2024/Revised 19 March 2024/Accepted 16 April 2024/Published online 19 August 2024

Abstract Causation promotes the understanding of correlation to an advanced stage by elucidating its underlying mechanism. Although statisticians have specified the possible causal relations among correlations, inferring causal structures is impossible from only the observed correlations in the classical world. Quantum correlations encapsulating the most defining aspects of quantum physics have taken a new turn for the causal inference problem — the two-point spatial and temporal quantum correlations with observationally discernible characteristics correspond exactly to the two most basic causal structures. However, a direct causal interpretation for quantum correlations has only been established in very limited cases. Here, we explore to what extent quantum correlations promote causal inference. Theoretically, we have found that the distinguishable causal regime of two-point Pauli correlations can be expanded from a single value to an asymmetric interval, and the causal structures determining the quantum correlations can be interpreted by a simple distance criterion. Experimentally, we have devised and implemented a versatile non-unital quantum channel in an optical architecture to directly observe such an asymmetric interval. The setup enabled quantum causal inference without any requirement of active intervention, which is impossible in the classical realm. Our work facilitates the identification of causal links among quantum variables and provides insight into characterizing causation and spatial-temporal correlation in quantum mechanics.

Keywords causality, quantum information, quantum channel, channel-state duality, non-unital channel

1 Introduction

Identifying cause and effect has been one of the most significant objectives in modern science [1]; even the long-standing Reichenbach's principle [2] has pointed out the direction to consider this problem: any observed correlation between two variables can be explained by a direct cause or an unobserved latent variable acting as the common cause. It is still impossible to distinguish between these two fundamental causal structures without the assistance of tools like interventions and instrumental variables [3–5]. All these causal discovery approaches assume access to additional resources beyond observational data; however, this may not be the case in many scenarios like determination of virus contagiousness [6, 7] and drug efficacy [8–10] in a pandemic era. Hence, using fewer resources to dig out the in-depth causal relationship between variables from the observed correlation data is a significant task with potentially broad interdisciplinary applications.

On causal discovery in the quantum realm, the simplest quantum correlations that imply the two basic causal structures are the two-point temporal quantum correlation (TQC) and spatial quantum

* Corresponding author (email: zhikuan.zhao@inf.ethz.ch, yushang@mail.ustc.edu.cn, tjs@ustc.edu.cn, cfi@ustc.edu.cn)

correlation (SQC), the former is obtained by measuring two observables at two ends of a quantum channel and the latter by measuring two observables at each part of a bipartite system. A counter-intuitive phenomenon is that it is possible to infer causal structures of quantum correlation with only observational data [11]: the two-point TQC and SQC exhibit different parity in the vicinity of the correlation polytopes' extremals [12]. This causal inference of these two quantum correlations hinges on the unique feature of the quantum system: for TQC, it originates from the coherence owned by the quantum unitary channel, and for SQC, the maximal entangled state presented by the bipartite state [13]. However, despite quantum causal modeling is currently a vibrant research frontier with significant theoretical [14–20] and experimental [21–25] progress, to what extent the quantum feature in causal inference sustains in practical settings, e.g., in correlations induced by non-unital channels due to the decoherence in a noisy intermediate-scale quantum [26] network or non-maximally entangled state, is poorly understood.

To address this question, we first start with a full characterization of two-point quantum correlations. The study of the discrepancies between TQCs and SQCs [27,28] has been a continuous topic of experimental interest [29,30]. As there is no analog to the monogamy of entanglement [31] governing TQCs [32,33], multi-point TQCs exhibit a richer behavioral scope than the spatial one [34–36], rendering TQCs indispensable for the interpretation of specific observed statistics [37]. In a preceding work [38], one of us authors also showed that the sets of two-point TQC and SQC do not have a one-to-one correspondence. Therefore, the parity of correlations fails to capture the essence of causal structures in general cases, in contrast to the extremal cases in [11].

Taking such an asymmetry into account, here we have thoroughly analyzed the implication of two-point quantum correlations to infer their causal structures. We have implemented an optical experiment to directly observe the asymmetric domains of spatial-temporal Pauli correlations and their influence on causal discovery. Our main technical contribution is the systematic realization of a fully-controlled photonic non-unital channel which, together with a non-maximally-mixed input state, suffice to activate the asymmetry between SQC and TQC. We also visualized this asymmetry with a geometrical representation of two-point Pauli correlations [38–41]. Furthermore, in the same vein of this geometrical viewpoint, we used a metric based on Euclidean distance to classify TQC and SQC, and explore their utility as a causal witness to link quantum correlations and causation. Although the experiment here only involves two-point quantum correlations, the experimental method is highly general, modular and standardized, thus applicable in the investigation of multi-point correlations in higher-dimensional systems. Therefore, we envision that our photonic experiment will facilitate the investigation of quantum correlations and causality in practical quantum networks in the near future.

2 Results

2.1 Observational quantum causal discovery

Our aim in this paper is to distinguish between the two paradigms of basic quantum causal structures, namely, the direct cause engendering TQCs and the common cause giving rise to SQCs, using only observational statistics. The scenario is best explained by a quantum comb representation [42]. Explicitly, Figure 1(a) describes a TQC generated from a single-qubit state ρ_0 that evolves into a completely positive trace-preserving (CPTP) map $\varepsilon_{B|A}$, whereas Figure 1(b) describes a SQC generated from two subsystems connected by a two-qubit state ρ_{AB} . Both the two-point TQC and SQC are obtained by measuring the Pauli operators σ_i^A and σ_j^B with $i, j \in \{1, 2, 3\}$ and extracting the statistics restored at the reservoirs R_A and R_B .

In general, observational causal discovery is intractable for classical correlations because a properly chosen latent variable acting as a common cause can nevertheless explain the correlations from a direct cause structure. Consequently, although the measurement of σ_i^A temporally precedes that of σ_j^B , the nature of the cause and effect between the two events are not a priori known, and additional resources like active intervention or instrumental variables are required for deducing causation. However, the diverse behaviors of quantum correlation enable the observational causal discovery between quantum observables. Our objective is to determine whether the two-point correlation $\langle \sigma_i^A \sigma_j^B \rangle$ is temporal (induced by a CPTP channel) or the correlation is spatial (compatible with a bipartite state), as the gray shades in Figure 1(c).

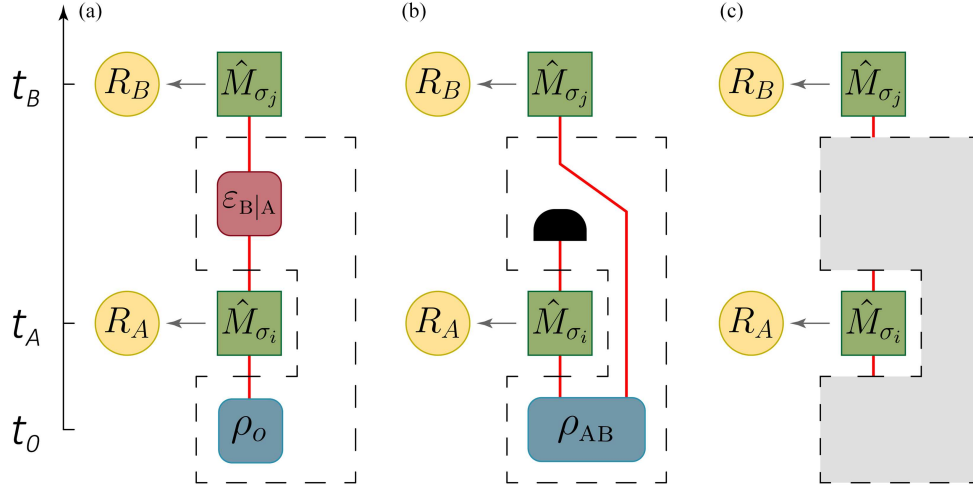


Figure 1 (Color online) Inferring causal structure from quantum correlations in space-time. (a) The two-point TQC. A single qubit ρ_0 is measured at two instances in time, t_A and t_B , by two Pauli measurements, \hat{M}_{σ_i} and \hat{M}_{σ_j} , with a CPTP map $\varepsilon_{B|A}$ between them. The measurements collapse the qubit according to Lüder's rule [43]. The results are stored in two reservoirs R_A and R_B and retrieved later to extract the correlation. (b) The two-point SQC. The two-qubit state ρ_{AB} are successively measured at time instances t_A and t_B by two Pauli measurements \hat{M}_{σ_i} and \hat{M}_{σ_j} , respectively. The evolutions of the two subsystems after preparation occur independently of one another. (c) The simplest task in the quantum causal inference is to identify whether the statistical two-point quantum correlation of the quantum comb is a TQC induced by a direct causal link or a TQC induced by a quantum common cause.

To exemplify the quantum feature, we focus upon a subset of two-point Pauli correlations,

$$\{\langle \sigma_1^A \sigma_1^B \rangle, \langle \sigma_2^A \sigma_2^B \rangle, \langle \sigma_3^A \sigma_3^B \rangle\}.$$

The correlations in the temporal domain are generated by two sequential measurements: the first measurement σ_i^A with outcome ± 1 causes the quantum state to collapse as $\rho_0 \rightarrow \rho'_\nu = (\mathbb{I} + \nu \sigma_i)/2$, $\nu = \pm 1$ [43]; subsequently, the quantum channel is applied on the collapsed state and the second measurement σ_i^B is cast after the channel operation. The resulting TQC read

$$\langle \sigma_i^A \sigma_i^B \rangle_t := \sum_{\nu=\pm 1} \text{Tr} \left(\rho_0 \frac{\mathbb{I} + \nu \sigma_i}{2} \right) \text{Tr} [\varepsilon_{B|A}(\rho'_\nu) \sigma_i]. \quad (1)$$

As shown in Supporting information and [38], these correlations can be further evaluated as

$$\langle \sigma_i^A \sigma_i^B \rangle_t = \text{Tr} [\varepsilon_{B|A}(\sigma_i) \sigma_i + \langle \sigma_i \rangle_{\rho_0} \varepsilon_{B|A}(\sigma_0) \sigma_i], \quad (2)$$

where $\sigma_0 = \mathbb{I}$ is the identity matrix, and $\langle \sigma_i \rangle_{\rho_0} = \text{Tr}(\rho_0 \sigma_i)$ is a shorthand for the expectation of the Pauli matrix σ_i on the state ρ_0 . On the other hand, for the correlations in the spatial domain, an SQC is simply the Pauli correlations of a bipartite system:

$$\langle \sigma_i^A \sigma_i^B \rangle_s := \text{Tr} [\rho_{AB} (\sigma_i^A \otimes \sigma_i^B)]. \quad (3)$$

Our first observation for an observational quantum causal discovery is that the spatial and temporal Pauli correlations have different parities. Indeed, the four Bell states are the common eigenstates of the three Pauli product operators, each with the product of the three eigenvalues being $C := \prod_{i=k}^3 \langle \sigma_k^A \sigma_k^B \rangle = -1$; whereas the Pauli channels $\rho \rightarrow \sigma_i \rho \sigma_i$ cause the product of the three correlations to be $C = +1$ due to the Pauli operators being anti-commutative and involutory. In [11], the authors have exploited this property of spatial-temporal correlations to realize a causal inference in the above extremal cases.

With the above parity criterion, only some very contrived causal relations can be distinguished; furthermore, the criterion is not robust against any noise. To address these issues and put the unique quantum feature in causal discovery into a pragmatic context, we use the three two-point Pauli correlations to form a set of coordinators in the Euclidean space. This geometric perspective actually supplies the generality and robustness. Starting by considering the spatial domain, the Pauli SQC of any two-qubit state can

be obtained from its expansion on the Bell states; it is but the average of the Bell states' correlations weighed by the moduli of the expansion coefficients. Therefore, in the geometric picture, all SQCs fall in a tetrahedron with odd-parity vertices $\{(-1)^m, (-1)^n, (-1)^{1+m+n}\}$, $m, n \in \{0, 1\}$ corresponding to the Bell states [44, 45].

The situation in the temporal domain is comparatively more complicated. The first term of (2) is a direct analogue of (3), so when the second term of this (2) vanishes, the set of TQCs reduces to a tetrahedron \mathcal{T}_t with its vertices given by even-parity coordinates, $\{(-1)^m, (-1)^n, (-1)^{m+n}\}$. Physically, this requirement can be specified as either the initial state ρ_0 is maximally mixed, or the channel is unital ($\varepsilon_{B|A}(\mathbb{I}) = \mathbb{I}$). The parity difference between \mathcal{T}_t and \mathcal{T}_s originates from the renowned Choi-Jamiołkowski isomorphism, which sets a one-to-one correspondence between an arbitrary quantum channel and a bipartite quantum state

$$\rho_{AB}^{\text{Choi}}(\varepsilon_{B|A}) = \left(\mathcal{I}_A \otimes \frac{\varepsilon_{B|A}}{2}\right) \sum_{ij} |ii\rangle\langle jj|_{AB}, \quad (4)$$

where \mathcal{I}_A denotes the identity super-operator acting on the first subsystem. With the Choi-Jamiołkowski isomorphism, every TQC induced by a given channel, with a maximally-mixed input state, can be calculated as

$$\langle \sigma_i^A \sigma_i^B \rangle_t = \text{Tr} \left[\rho_{AB}^{\text{Choi}}(\varepsilon_{B|A})^{\text{PT}} (\sigma_i^A \otimes \sigma_i^B) \right],$$

where PT indicates partial transpose over the first subsystem. This partial transpose causing a geometrical symmetry about the $\langle \sigma_2^A \sigma_2^B \rangle = 0$ plane between \mathcal{T}_t and \mathcal{T}_s accounts for the parity difference between \mathcal{T}_t and \mathcal{T}_s . However, when the second term of (2) is non-zero, the conditional symmetry from the Choi-Jamiołkowski isomorphism breaks down. In [38], one of us authors has shown that under this circumstance, the TQCs stuff a dilated tetrahedron with the same vertices as \mathcal{T}_t , denoted as \mathcal{Q}_t . Its surfaces are described by the following parametric equations:

$$\begin{aligned} \langle \sigma_1^A \sigma_1^B \rangle &= \cos(u), & \langle \sigma_2^A \sigma_2^B \rangle &= \cos(v), \\ \langle \sigma_3^A \sigma_3^B \rangle &= \cos(u - v), & u \in [0, 2\pi], v \in [0, \pi]. \end{aligned}$$

In Section 4, we further show that the surfaces of \mathcal{Q}_t can be efficiently encompassed with a family of photonic non-unital channels acting upon a pure input state. Next, we proceed to the experimental implementation of the non-unital evolution and characterization of the bounding set, \mathcal{Q}_t .

2.2 Experiment

Our photonic setup realizing the non-unital channel is depicted in Figure 2. The single photon's polarization degree of freedom is used to register the qubit, with $|H\rangle$ ($|V\rangle$) denoting the horizontal (vertical) polarization state. In the preparation stage, heralded, $|H\rangle$ -polarized single photons are generated by pumping a poled potassium titanyl phosphate (ppKTP) crystal. After the first projection of σ_i^A (at time t_A) using a group of the half-wave plate (HWP) and quart-wave plate (QWP), the measurement result is stored in the orbital angular momentum (OAM) using a spatial light modulator (SLM) temporarily. The second group of HWP and QWP is used to revert the polarization of the photons. Subsequently, we implement the non-unital channel $\varepsilon_{B|A}$ to refactor the two-point TQC beyond the paradigmatic \mathcal{T}_t . The second projection measurement σ_i^B (at time t_B) is achieved by the last pair of HWP and QWP as well as a polarization beam splitter (PBS). Finally, after the sequential measurements, the photons of different post-measurement states are split into four spatial modes by two SLMs, which are then collected by four single-photon avalanche detectors (SPADs). The coincidence counting rates at the four exits with the trigger photon reveal the desired TQC, $\langle \sigma_i^A \sigma_i^B \rangle$ (here and after we omit the subscript for convenience). The details of the experimental setup are given in the Methods section.

We first work with the geometrical picture to illustrate the symmetry and asymmetry between the set of TQC and SQC. As presented in Figure 3(a), the restricted set of TQCs with a vanishing second term of (2), \mathcal{T}_t , is represented by a red tetrahedron; its spatial counterpart \mathcal{T}_s is reflected about the plane $\langle \sigma_2^A \sigma_2^B \rangle = 0$, and is represented by the blue tetrahedron. The set of all possible TQCs is depicted by the red translucent "inflated tetrahedron", \mathcal{Q}_t . Compared with the \mathcal{T}_t inside it, the inflated \mathcal{Q}_t inscribes a volume that is approximately 85% larger, which manifests additional allowable correlation statistics. For example, at the face centers of \mathcal{Q}_t , the parity indicator $C = -\frac{1}{8}$ reaches its minima, smaller than $C = -\frac{1}{27}$ obtained at the face centers of \mathcal{T}_t . Moreover, \mathcal{Q}_t has some partial overlap with \mathcal{T}_s in addition

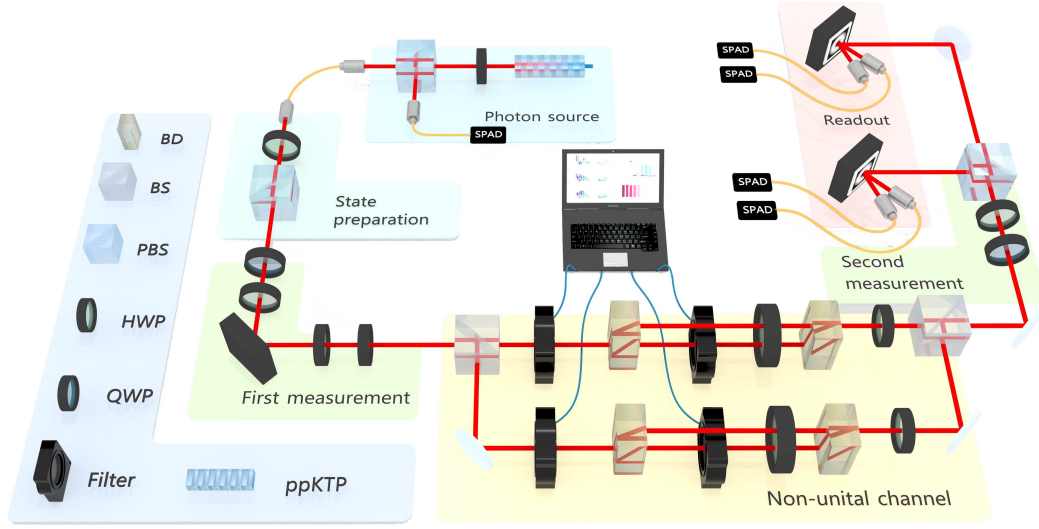


Figure 2 (Color online) Experimental setup. Ultraviolet continuous-wave laser pumped a periodically ppKTP crystal to produce polarization-entangled photon pairs. The first SLM encoded the measurement outcomes in the spatial profiles of the photons and the basis of the first measurement is selected by a set of wave plates. After another set of wave plates recovered the initial polarization of the photon, it entered the non-unital channel implemented by an unbalanced Mach-Zehnder interferometer. Then, the polarization state of the photon was measured again by wave plates and PBS. Two SLMs transformed different spatial modes of the signal photon into different propagating directions. Finally, the photos were detected by SPADs at the four exit angles.

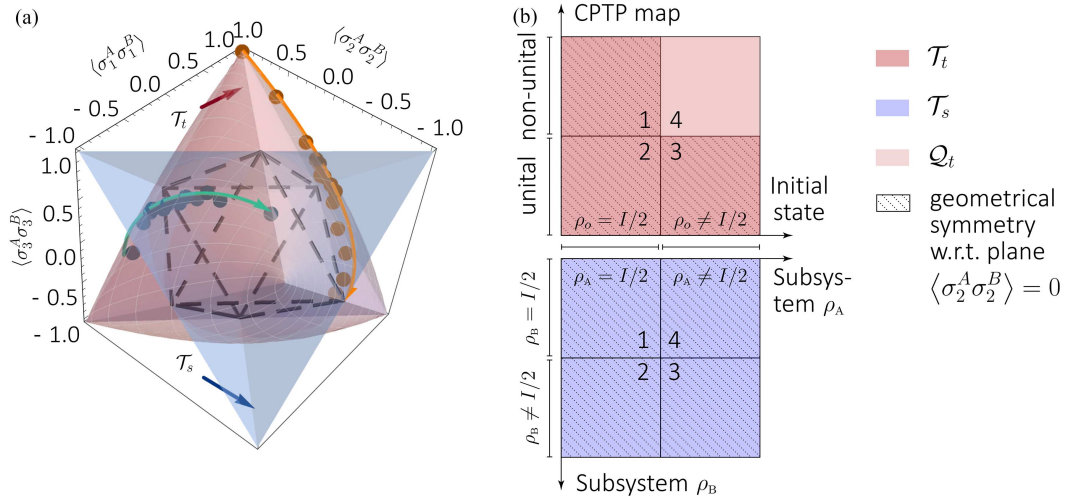


Figure 3 (Color online) Geometry of two-point quantum correlations. (a) The red tetrahedron \mathcal{T}_t describes the two-point TQC conditioned on a maximally mixed initial state or unital channel evolution, whereas the blue tetrahedron \mathcal{T}_s describes the two-qubit SQC. They are symmetric about the $\langle \sigma_2^A \sigma_2^B \rangle = 0$ plane. The red translucent “inflated tetrahedron” \mathcal{Q}_t encircling \mathcal{T}_t represents all sets of TQC resulted by a non-unital channel between two single-qubit measurements. The orange- and cyan-coloured points represent the experimental results of the two typical parametric Kraus operators with $v = 2u$ and $u \in [0, \pi/2]$, and $u = 2\pi/3$ and $v \in [0, 2\pi/3]$, respectively; the two curves correspond to the theoretical predictions. The 3σ error bars are too small to be displayed. (b) Schematic illustration of the duality between TQC and SQC. Upper: dependence of TQC upon the mixedness of the initial state ρ_0 (horizontal axis) and the unitality of the CPTP map (vertical axis). Lower: dependence of SQC upon the mixedness of the two marginal states, $\rho_A = \text{Tr}_B[\rho_{AB}]$ and $\rho_B = \text{Tr}_A[\rho_{AB}]$. The regions with dashed diagonal lines exhibit geometrical symmetry between \mathcal{T}_t and \mathcal{T}_s in Euclidean space.

to the octahedral region $\mathcal{O}_s = \mathcal{T}_s \cap \mathcal{T}_t$, which physically represents the SQC that is generated by the two-qubit separable states [44, 45].

The above analysis was best illustrated by our experimental results. We chose two trajectories as instances on the surface of \mathcal{Q}_t represented by the orange and cyan theoretical curves in Figure 3(a) and investigate the quantum correlation functions of these two exemplary curves, i.e., $C \equiv \prod_{i=1}^3 \langle \sigma_i^A \sigma_i^B \rangle$ [11]. By adjusting the parameters of the quantum channel, we obtained the orange and cyan points selected from these two sets of groups and investigated the detailed information of states in experiments. We

found that after the evolution of the non-unital channels, most of the points lay outside \mathcal{T}_t , and the maximal distance of the data points from the nearest surface of \mathcal{T}_t was 0.250 ± 0.014 , falling just slightly short of the theoretical maximum of $\sqrt{3}/6$ because of experimental imperfections. The data point at coordinates $(-0.493, 0.515, 0.427)$ yielded a parity indicator of $C = -0.108$ very close to the theoretical lower bound of TQC-allowed domain, $[-\frac{1}{8}, 1]$. We see that the introduction of the non-unital channel breaks the symmetry in statistics of C between direct cause effects ($C \in [-\frac{1}{27}, 1]$) and common cause effects ($C \in [-1, \frac{1}{27}]$) [12]. The standard deviation of the distance measure is numerically estimated via Monte Carlo simulation. More information of the 3D plots is presented in Supporting information.

We now switch to another legible perspective displayed in Figure 3(b) to further expound the relationships between \mathcal{Q}_t , \mathcal{T}_t and \mathcal{T}_s . Here, the upper red square categorizes the possible sets of two-qubit TQCs, (1), according to different combinations of initial state and quantum channel, which together span \mathcal{Q}_t in Figure 3(a). The lower blue square classifies the possible sets of two-point SQCs, (3), captured by the blue tetrahedron, \mathcal{T}_s in Figure 3(a), with different cases of marginal states $\rho_A = \text{Tr}_B[\rho_{AB}]$ and $\rho_B = \text{Tr}_A[\rho_{AB}]$. First, due to the Choi-Jamiołkowski isomorphism (4) mapping any quantum channel to a bipartite quantum state with one of the subsystem being maximally mixed, the TQCs induced by a maximally mixed initial state corresponding to the red squares 1+2 conjugate with the SQCs from a one-side maximally mixed two-qubit system corresponding to the blue squares 1+2. As the Bell states all have maximally mixed marginal states, the blue square 1 already gives all possible SQCs. Second, according to the form of (2), the set of TQCs from an arbitrary initial state ρ_0 subjected to an unital channel (red squares 2+3) equals which caused by a maximally mixed initial state $\rho_0 = \mathbb{I}/2$ subjected to an arbitrary choice of the quantum channel (red squares 1+2). This concludes our analysis that the concurrence of a non-maximally mixed input state and the non-unital channel (small red square 4) produces non-trivial TQCs with no SQCs as analog.

2.3 Causal influences

Knowing the asymmetry between TQCs and SQCs, we are now in a position to quantify the domains of spatial-temporal correlations and realize a robust observational causal inference. Going beyond the paradigm of the parity criterion [11], our geometric method is capable of identifying a large class of causal relationships. Here, we focus on a very characteristic region of correlations, $(\mathcal{Q}_t \setminus \mathcal{T}_t) \cap \mathcal{T}_s$. As already discussed in Subsection 2.2, no previous parity criteria overlooking the effect of non-unital channels can correctly explain the origin of such correlations. To the best of our knowledge, the causal structure of this region has been little investigated. In this case, further tools are required to reveal the underlying causality and quantify the two-point quantum correlations.

For the inquiry of causal influence, we now define some useful quantities borrowed from the concepts of quantum entanglement. For an unknown-type quantum correlation represented by a point in the geometric picture, the witness of spatial correlation, \mathcal{SC} , is defined as its signed Euclidean distance to the nearest facet of \mathcal{T}_s ; the witness of entanglement, \mathcal{EW} , is defined as the Euclidean distance between the point and the nearest point of the octahedron \mathcal{O}_s [46]. When the point is inside the polyhedron, the corresponding witness is positive. Furthermore, to faithfully certify the TQC, we resort to the pseudo-density matrix (PDM) (Supporting information and [39]) formalism of the two-point correlation. The formal definition of the PDM, R , is given in Section 4; note that the PDM contains inhomogeneous Pauli correlations $\langle \sigma_j^A \sigma_k^B \rangle, j \neq k$ and is obtained via tomographic reconstruction. In this language, the negativity of temporal correlation is defined as $\mathcal{TC} = \|R_{AB}\|_{\text{tr}} - 1$, and a nonzero \mathcal{TC} indicates the two-point correlation must interpreted as a TQC (Supporting information and [39]).

We use the above-defined quantities to analyze the causal aspects of the experimental data points in Figure 3(a). The results are shown in Figure 4. The green, blue and red curves correspond to the theoretical \mathcal{TC} , \mathcal{SC} and \mathcal{EW} values of the states, respectively. We see that in both sets of states, $\mathcal{TC} > 0$ was satisfied by all data points, confirming a direct cause origin of the correlations. In Figure 4(a), wherever $u > 0.90$ rad, $\mathcal{SC} > 0$, so the TQC and SQC were not distinguishable solely through statistical analysis of the Pauli correlations $\langle \sigma_i^A \sigma_i^B \rangle$. The same phenomenon can be observed in Figure 4(b) when 0.75 rad $< v < 1.33$ rad. Note that when both $\mathcal{TC} > 0$ and $\mathcal{SC} > 0$, the latter can serve as a witness of a quantum non-unital channel as no TQCs located in the region $(\mathcal{Q}_t \setminus \mathcal{T}_t)$ could be induced by an unital channel. Furthermore, the entanglement witness \mathcal{EW} went as low as -0.237 ± 0.016 , indicating that these TQCs generated by our experimental non-unital channel can mimic the correlations of two-qubit entangled states. From the geometrical picture, the imitation of entangled-state statistics is evidently

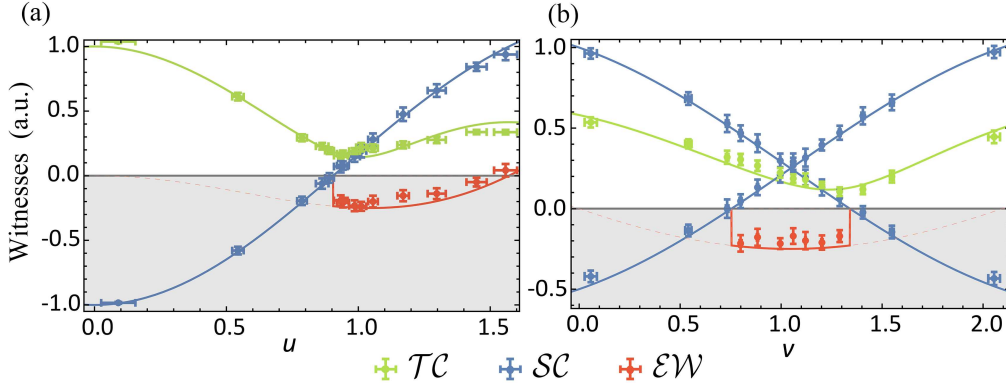


Figure 4 (Color online) Quantified results for the correlations and the entanglement witness. (a) and (b) correspond to the orange and cyan points in Figure 3, respectively, and each data point corresponds to an experimental PDM R or three Pauli correlations $\langle \sigma_i^A \sigma_i^B \rangle$ acquired from the measurements of a qubit at two time instances. The horizontal coordinates denote the parameters of the corresponding channel. The blue lines represent the theoretical SQC values, SC , of the states. There are two SC functions in (b) because the points in this case need to be bounded by two functions. The green points are the TQC values of the states, and the red points are the experimental EW s, calculated only for those states satisfying $SC > 0$. The data points of each color represent the corresponding experimental values, and the error bars represent the 3σ standard deviation.

not achievable using only the unital channels. Therefore, our experiment has demonstrated an advantage of the non-unital channel in quantum information tasks.

It is interesting to remark that the existence of direct causal links logically implies signaling, i.e., information is passed forward in time, which intuitively motivated a bound for quantum channel capacities based on quantifying temporal correlations in [47]. Indeed, such ability to signal is part and parcel of the distinction between TQC and SQC, and therefore ultimately responsible for the difference in the bounding sets for the temporal and spatial scenarios. Here we have seen that, as a result of the broken symmetry there is an overlapping region of allowable two-point TQCs and SQCs $(\mathcal{Q}_t \cap \mathcal{T}_s) \setminus \mathcal{O}_s$, which allows for temporal signaling to mimic statistics produced by spatial entanglement and vice versa, albeit not maximally in either case.

3 Methods

3.1 Detailed experiment setup

In our experiment, a photonic setup is adopted to generate a non-unital evolution on a single-qubit state and implement two temporal measurements at two ends of the channel in order to extract the two-point TQC. The detailed experimental setup has been shown in the main text as Figure 2. It contains the following components: photon source, state preparation, first measurement, the non-unital channel evolution, second measurement, and results readout. Here, we give a detailed account of the techniques used in our experiment. A periodic ppKTP crystal is pumped by an ultraviolet continuous-wave laser with a central wavelength of 404 nm to generate heralded single photons with a central wavelength of 808 nm through type-II spontaneous parametric down-conversion. An interference filter (not shown in the figure) is inserted to remove the residual pumping light.

3.1.1 First measurement

The application of the first SLM in this step is to register the outcome of the first polarization measurement, implemented by the first group of QWP and HWP, into the OAM degree of freedom. Throughout this subsection, we denote the state of the photon by the tensor product of its polarization state and OAM state. The computational basis are related to the polarization state by the correspondence $|0\rangle^{\text{pol}} \leftrightarrow |H\rangle, |1\rangle^{\text{pol}} \leftrightarrow |V\rangle$ with $|H\rangle$ and $|V\rangle$ denoting the horizontal and vertical polarization of the photon, and to the OAM state by $|0\rangle^{\text{OAM}} \leftrightarrow |\ell = 0\rangle, |1\rangle^{\text{OAM}} \leftrightarrow |\ell = +2\rangle$ with ℓ denoting the OAM charge (modulo \hbar) of the photon.

To achieve this non-demolition measurement of the polarization state it is enough to cast a controlled-NOT gate from the polarization qubit to a blank OAM state. The gate is based on the polarization-sensitive nature of the SLM: it only imprints the phase of the hologram onto vertically-polarized photons.

Therefore, measurement of σ_i^A can be achieved by first casting a polarization unitary $|H\rangle\langle\sigma_i^+| + |V\rangle\langle\sigma_i^-|$, in which $|\sigma_i^\pm\rangle$ denotes the eigenstate of σ_i with an eigenvalue of ± 1 , then imprinting a spiral phase which adds an OAM charge of $\Delta\ell = +2$ on the photonic wavefunction, and finally reverting the polarization unitary with the second group of HWP and QWP. For an arbitrary polarization state $\alpha|\sigma_i^+\rangle + \beta|\sigma_i^-\rangle$, the first measurement effectively performs the controlled-NOT gate with the state conversion

$$(\alpha|\sigma_i^+\rangle + \beta|\sigma_i^-\rangle)^A |0\rangle \rightarrow \alpha|\sigma_i^+\rangle^A |0\rangle + \beta|\sigma_i^-\rangle^A |1\rangle.$$

After the measurement, the OAM state $|0\rangle^{\text{OAM}}$ is carried by a zeroth-order Gaussian mode and $|1\rangle^{\text{OAM}}$ is carried by a co-propagating second-order Laguerre-Gaussian mode.

3.1.2 Photonic non-unital channel

After finishing the first measurement procedure, the photon enters into the non-unital channel step. This realization forms the principal contribution of our experimental work. The completely positive requirement enables some sets of possible channel $\varepsilon_{B|A}$ to be trigonometrically polarized in the Pauli basis, and can be characterized by the Kraus operators [48, 49]:

$$\begin{aligned} K_+ &= \left[\cos \frac{v}{2} \cos \frac{u}{2} \right] \sigma_0 + \left[\sin \frac{v}{2} \sin \frac{u}{2} \right] \sigma_3 \\ &= \begin{pmatrix} \cos \frac{v-u}{2} & 0 \\ 0 & \cos \frac{v+u}{2} \end{pmatrix}, \end{aligned} \quad (5)$$

$$\begin{aligned} K_- &= \left[\sin \frac{v}{2} \cos \frac{u}{2} \right] \sigma_1 - i \left[\cos \frac{v}{2} \sin \frac{u}{2} \right] \sigma_2 \\ &= \begin{pmatrix} 0 & \sin \frac{v-u}{2} \\ \sin \frac{v+u}{2} & 0 \end{pmatrix}, \end{aligned} \quad (6)$$

where $v \in [0, \pi]$, $u \in [0, 2\pi]$. The effect of this CPTP channel applied on an arbitrary single qubit in state ρ is $\varepsilon_{B|A}(\rho) = K_+ \rho K_+^\dagger + K_- \rho K_-^\dagger$, which maps the family of density operators from the state space \mathcal{H}_A at time t_A to the state space \mathcal{H}_B at time t_B . Observe that from the definition of the Kraus operators, the matrix form of K_+ (5) will have only real terms in the diagonal entries and K_- (6) will have only real terms in the off-diagonal entries in the computational basis. The mathematical form of the Kraus operators inspires us to construct the non-unital evolution by first implementing two qubit non-unital channels with diagonal matrix form, i.e., $K_+ \rho K_+^\dagger$, then apply on one of them a σ_x transformation to switch to evolution with off-diagonal form, i.e., $K_- \rho K_-^\dagger$, and finally synthesize the non-unital channel from the probabilistic mixture of the two subchannels.

Experimentally, the non-unital channel is constituted by an unbalanced Mach-Zehnder interferometer, with the photonic wavefunction undergoing the K_+ (K_-)-induced evolution in the upper (lower) arm of the interferometer. The length difference between the two arms is about 20 cm, which is much longer than the coherence length (≈ 0.2 mm) of the photons used in the experiment; this way, the coherence between the two arms is destroyed and the output of the unbalanced Mach-Zehnder interferometer can be expressed by two Kraus operators. For the range of parameters u, v that we are interested in, the matrix element in the second row (which is applied on the $|V\rangle$ -polarized photonic wavefunction) of both K_+ and K_- will have no greater absolute values than the one in the first row (which is applied on the $|H\rangle$ -polarized photonic wavefunction). Therefore, an amplitude filtering on the $|V\rangle$ -polarized photons suffices to realize the K_+ -induced evolution up to a renormalization of the wavefunction [50]; together with an HWP oriented at 45° the K_+ -induced evolution can also be implemented.

The neutral density filters (NDs) are used to induce a decrease of the wavefunction amplitude corresponding to the photons on a specific path. We use two sets of beam displacers (BDs) to separate and re-combine the propagating paths of the $|H\rangle$ - and $|V\rangle$ -polarized photons, and add an adjustable density filter on the path of the $|V\rangle$ -polarized photons to induce the on-demand amplitude damping. We also add an HWP with its optical axis oriented at 45° (0°) in the lower (upper) arm of the unbalanced interferometer to induce the σ_x transformation necessary for the K_- Kraus operator, and two adjustable density filters in both arms before the BDs to compensate the amplitude ratio before the K_+ and K_- subchannels. The four filters are installed on motorized rotation stages controlled by a lab computer, and programmed to conduct the precise control of our non-unital channel parameters u, v with high precision.

3.1.3 Second measurement and extraction of TQC

At this stage, the photons have finished the non-unital evolution, and we make the second measurement to extract the desired TQCs. The second measurement is a joint measurement on the polarization and OAM degrees of freedom. The measurement of the polarization state σ_i^B is a standard projective measurement implemented by a set of wave plates and a PBS; the orientations of the wave plates are selected such that the $+1(-1)$ eigenstate of σ_i , viz, $|\sigma_i^+\rangle$ ($|\sigma_i^-\rangle$), is rotated to $|H\rangle$ ($|V\rangle$) and pass through (is reflected by) the PBS.

The measurement of the OAM state that now carries the information of σ_i^A , on the other hand, is based on the observation that a photon carries nonzero OAM charge $\ell \neq 0$ cannot be collected by a single-mode fiber due to their orthogonal spatial modes. We put two SLMs on the two outbound paths of the PBS to implement the OAM state discrimination, with one HWP oriented at 45° inserted before one of the SLMs so it can modulate horizontally-polarized photons. The phase holograms displayed on the SLM are comprised of two parts: a blazed grating in the central area that deflect the photons with $|\ell = 0\rangle$ to the left, and a forked grating in the peripheral area that deflects the photons with $|\ell = +2\rangle$ to the right and add an OAM charge of $\Delta\ell = -2$ to these photons. The photons, now propagating along different directions according to their initial OAM state, are collected by four SPADs (two for each polarization state) whose counting rates give the detection probabilities on a specific basis. Although the intensity profiles of $|\ell = 0\rangle$ and $|\ell = +2\rangle$ photons are not completely separated and some photons in the transition area may be deflected to the opposite direction, they will have nonzero OAM charge at the fiber coupler and consequently cannot contribute to the counting events. The separation of $|\Delta\ell| = 2$ provides decent orthogonality between the two spatial modes and the extinction ratio between the two OAM modes is estimated to be above 10^4 . To guarantee the collection efficiency of the $l = 0$ and $l = 2$ modes to be the same, we have used an adjustable collimator and fine-tuned the distance between it and the fiber tip. We have measured the counting rate of the two bases and the difference is within 2%.

The probabilities of different measurement outcomes are obtained by normalizing photon counts in certain paths to the total photon counts. Here, we denote the probabilities by $p_{AB}^{\pm\pm}$, where the two superscripts denote the outcomes of the first and second measurements. With these four probability distributions at hand, we can calculate the expectation value of the correlation as

$$\begin{aligned} \langle \sigma_i^A \sigma_i^B \rangle &= (+1) \times (+1) \cdot p_{AB}^{++} + (+1) \times (-1) \cdot p_{AB}^{+-} \\ &\quad + (-1) \times (+1) \cdot p_{AB}^{-+} + (-1) \times (-1) \cdot p_{AB}^{--} \\ &= p_{AB}^{++} + p_{AB}^{--} - p_{AB}^{+-} - p_{AB}^{-+}. \end{aligned} \quad (7)$$

Because we have adopted four SPADs to record the counting rates of all four possible combinations of the two-qubit measurements, the normalization of detection probabilities can be made within an orthonormal basis and does not span over different settings of the non-unital channel and different phase masks displayed by the SLM, making the recorded statistics more robust against possible experimental imperfections.

3.2 PDM

The PDM formalism introduced in [39] is particularly useful for more deeply investigating into the relationship between TQC and SQC in the overlapping region. A two-point PDM is determined by the expectation values of all combinations of two-point Pauli measurements on the qubit: $R_{AB} := \frac{1}{4} \sum_{j=0}^3 \sum_{k=0}^3 \langle \sigma_j^A \sigma_k^B \rangle \sigma_j^A \sigma_k^B$. To this end, we experimentally measure all of the correlations of the dark orange and cyan points in Figure 3(a) and deduce the PDM using quantum-state tomography, which allows for computation of a scalar measure of causality based on the trace norms of the PDM: $\mathcal{TC} = \|R_{AB}\|_{\text{tr}} - 1$, and $\|R_{AB}\|_{\text{tr}}$ represent the sums of the singular values of the PDM.

4 Conclusion

We have investigated the cause and effect relation in two-point quantum correlations which has several drastically different properties from the classical cases. First, we gave a geometrical illustration of the bounding sets of the two-point temporal and SQC and observed an inherent asymmetry between them by transferring a non-maximally mixed initial state into a specifically designed non-unital quantum channel.

The experiment results showed that the two-point TQC in three-dimensional space inscribes a volume 85% larger than the spatial one. Second, this asymmetry inspired us to apply the two-point spatial-temporal correlations in a robust observational causal inference scheme without introducing additional unnecessary uncertainties or disturbances. The observational scheme also has the practical advantage that it uses fewer resources than its interventional counterpart; for example, the measurement of \mathcal{TC} only requires 15 two-point correlations — less than one-quarter of a full causal tomography [11]. Third, using three causal quantifiers, we have directly measured the causal influences of the non-unital channel, and demonstrated that the observed statistics can mimic the correlations in the spatial domain to highlight the role of non-unitality in quantum information tasks.

Inferring causal relationships between variables is at the heart of any statistical inquiry. It was not until recently that the concept of cause and effect began to come into the quantum realm and the framework of quantum causality is gradually being refined. Although it has been widely accepted that classical correlation does not necessarily imply causation, the more profound physical connotation among quantum variables makes such a statement does not always hold for quantum correlation: the inherent non-classical properties of quantum systems such as quantum coherence and entanglement provide advantages in causal inferences for quantum variables, which endows people with the ability to acquire causality from correlations directly. With an experimental insight, our results provide support for such assertion. The geometric approach in this work could offer quantum variables with a novel perspective or even be generalized to the causal inferences of classical correlations. It can be further applied to provide people with a less consumed methodology to investigate the non-classicality of a quantum system or even be utilized to construct quantum causal networks upon quantum variable [51, 52].

Finally, our method is naturally applicable in measuring multi-point and qudit TQCs since it is feasible to record multiple TQCs into a single photonic OAM state. The OAM state has infinitely many eigenstates [53] which can be extracted simultaneously [54] to finish the registering task. Besides, our non-unital channel is implemented by an unbalanced Mach-Zehnder interferometer, so conventional optical elements are sufficient for adjusting its parameters with high precision. This devised and implemented versatile photonic non-unital channel can be extended to construct generic quantum channels with the arbitrary parameterization of Kraus operators, which may have applications in optical computing [55, 56] and the study of and non-Markovianity [57–59]. Also, by inducing amplitude damping, our specialized parametric non-unital quantum channel is capable of realizing equivalent photonic non-Hermitian evolution. Thus, our methodology may facilitate the investigation of the \mathcal{PT} -symmetric theory [60–62], quantum simulation based on adiabatic quantum computation [63], and enhance optical quantum sensing with non-Hermitian dynamics [64].

Acknowledgements This work was supported by Innovation Program for Quantum Science and Technology (Grant No. 2021ZD-0301200), National Natural Science Foundation of China (Grant Nos. 12174370, 12174376, 11821404, 11904356), Youth Innovation Promotion Association of Chinese Academy of Sciences (Grant No. 2017492), Open Research Projects of Zhejiang Lab (Grant No. 2021MB0AB02), Fok Ying-Tong Education Foundation (Grant No. 171007), Engineering and Physical Sciences Research Council and Quantum Computing and Simulation Hub (Grant No. T001062), and Fundamental Research Funds for the Central Universities (Grant No. WK2030000008).

Supporting information See supplementary information for more details about the derivation of (2), the quantum non-unital channels, and more perspective plots of the Figure 3. The supporting information is available online at info.scichina.com and link.springer.com. The supporting materials are published as submitted, without typesetting or editing. The responsibility for scientific accuracy and content remains entirely with the authors.

References

- 1 Pearl J, Mackenzie D. *The Book of Why: the New Science of Cause and Effect*. New York: Basic Books, 2018
- 2 Reichenbach H, Reichenbach M. *The Direction of Time*. Oakland: University of California Press, 1991
- 3 Morgan S L, Winship C. *Counterfactuals and Causal Inference*. Cambridge: Cambridge University Press, 2015
- 4 Imbens G W, Rubin D B. *Causal Inference in Statistics, Social, and Biomedical Sciences*. Cambridge: Cambridge University Press, 2015
- 5 Hernán M A, Robins J M. *Causal Inference: What If*. Boca Raton: Chapman & Hall/CRC, 2010
- 6 Baud D, Qi X, Nielsen-Saines K, et al. Real estimates of mortality following COVID-19 infection. *Lancet Infect Dis*, 2020, 20: 773
- 7 Viana R, Moyo S, Amoako D G, et al. Rapid epidemic expansion of the SARS-CoV-2 Omicron variant in southern Africa. *Nature*, 2022, 603: 679–686
- 8 Freedman N D, Park Y, Abnet C C, et al. Association of coffee drinking with total and cause-specific mortality. *N Engl J Med*, 2012, 366: 1891–1904
- 9 Lustig Y, Gonen T, Meltzer L, et al. Superior immunogenicity and effectiveness of the third compared to the second BNT162b2 vaccine dose. *Nat Immunol*, 2022, 23: 940–946

- 10 Regev-Yochay G, Gonen T, Gilboa M, et al. Efficacy of a fourth dose of Covid-19 mRNA vaccine against Omicron. *N Engl J Med*, 2022, 386: 1377–1380
- 11 Ried K, Agnew M, Vermeyden L, et al. A quantum advantage for inferring causal structure. *Nat Phys*, 2015, 11: 414–420
- 12 Hu M, Hou Y. Discrimination between quantum common causes and quantum causality. *Phys Rev A*, 2018, 97: 062125
- 13 Zhang C, Hou Y, Song D. Quantum observation scheme universally identifying causalities from correlations. *Phys Rev A*, 2020, 101: 062103
- 14 Allen J M A, Barrett J, Horsman D C, et al. Quantum common causes and quantum causal models. *Phys Rev X*, 2017, 7: 031021
- 15 Wood C J, Spekkens R W. The lesson of causal discovery algorithms for quantum correlations: causal explanations of Bell-inequality violations require fine-tuning. *New J Phys*, 2015, 17: 033002
- 16 Costa F, Shrapnel S. Quantum causal modelling. *New J Phys*, 2016, 18: 063032
- 17 Cavalcanti E G. Classical causal models for bell and kochen-specker inequality violations require fine-tuning. *Phys Rev X*, 2018, 8: 021018
- 18 Barrett J, Lorenz R, Oreshkov O. Quantum causal models. 2019. ArXiv:1906.10726
- 19 Wolfe E, Pozas-Kerstjens A, Grinberg M, et al. Quantum inflation: a general approach to quantum causal compatibility. *Phys Rev X*, 2021, 11: 021043
- 20 Pearl J C, Cavalcanti E G. Classical causal models cannot faithfully explain Bell nonlocality or Kochen-Specker contextuality in arbitrary scenarios. *Quantum*, 2021, 5: 518
- 21 Goswami K, Romero J. Experiments on quantum causality. *AVS Quantum Sci*, 2020, 2: 037101
- 22 Rubino G, Rozema L A, Feix A, et al. Experimental verification of an indefinite causal order. *Sci Adv*, 2017, 3: e1602589
- 23 Chaves R, Carvacho G, Agresti I, et al. Quantum violation of an instrumental test. *Nat Phys*, 2018, 14: 291–296
- 24 Yu S, Sun Y N, Liu W, et al. Realization of a causal-modeled delayed-choice experiment using single photons. *Phys Rev A*, 2019, 100: 012115
- 25 Agresti I, Poderini D, Polacchi B, et al. Experimental test of quantum causal influences. *Sci Adv*, 2022, 8: 1515
- 26 Preskill J. Quantum computing in the NISQ era and beyond. *Quantum*, 2018, 2: 79
- 27 Brukner C, Taylor S, Cheung S, et al. Quantum entanglement in time. 2004. ArXiv:quant-ph/0402127
- 28 Fritz T. Quantum correlations in the temporal Clauser-Horne-Shimony-Holt (CHSH) scenario. *New J Phys*, 2010, 12: 083055
- 29 Dressel J, Broadbent C J, Howell J C, et al. Experimental violation of two-party Leggett-Garg inequalities with semiweak measurements. *Phys Rev Lett*, 2011, 106: 040402
- 30 Fedrizzi A, Almeida M P, Broome M A, et al. Hardy's paradox and violation of a state-independent bell inequality in time. *Phys Rev Lett*, 2011, 106: 200402
- 31 Scarani V, Gisin N. Quantum communication between n partners and Bell's inequalities. *Phys Rev Lett*, 2001, 87: 117901
- 32 Streltsov A, Adesso G, Piani M, et al. Are general quantum correlations monogamous? *Phys Rev Lett*, 2012, 109: 050503
- 33 Toner B. Monogamy of non-local quantum correlations. *Proc R Soc A*, 2009, 465: 59–69
- 34 Leggett A J, Garg A. Quantum mechanics versus macroscopic realism: is the flux there when nobody looks? *Phys Rev Lett*, 1985, 54: 857–860
- 35 Budroni C, Moroder T, Kleinmann M, et al. Bounding temporal quantum correlations. *Phys Rev Lett*, 2013, 111: 020403
- 36 Costa F, Ringbauer M, Goggin M E, et al. Unifying framework for spatial and temporal quantum correlations. *Phys Rev A*, 2018, 98: 012328
- 37 Ringbauer M, Costa F, Goggin M E, et al. Multi-time quantum correlations with no spatial analog. *npj Quantum Inf*, 2018, 4: 37
- 38 Zhao Z, Pisarczyk R, Thompson J, et al. Geometry of quantum correlations in space-time. *Phys Rev A*, 2018, 98: 052312
- 39 Fitzsimons J F, Jones J A, Vedral V. Quantum correlations which imply causation. *Sci Rep*, 2015, 5: 18281
- 40 Zhang T, Dahlsten O, Vedral V. Quantum correlations in time. 2002. ArXiv:2002.10448
- 41 Kübler J M, Braun D. Two-qubit causal structures and the geometry of positive qubit-maps. *New J Phys*, 2018, 20: 083015
- 42 Chiribella G, D'Ariano G M, Perinotti P. Quantum circuit architecture. *Phys Rev Lett*, 2007, 101: 060401
- 43 Lüders G. Über die Zustandsänderung durch den Messprozeß. *Annalen der Phys*, 1950, 443: 322–328
- 44 Horodecki R, Horodecki M. Information-theoretic aspects of inseparability of mixed states. *Phys Rev A*, 1996, 54: 1838–1843
- 45 Horodecki M, Horodecki P, Horodecki R. Separability of mixed states: necessary and sufficient conditions. *Phys Lett A*, 1996, 223: 1–8
- 46 Mundarain D, Stephany J. Concurrence and negativity as distances. 2007. ArXiv:0712.1015
- 47 Pisarczyk R, Zhao Z, Ouyang Y, et al. Causal limit on quantum communication. *Phys Rev Lett*, 2019, 123: 150502
- 48 Beth Ruskai M, Szarek S, Werner E. An analysis of completely-positive trace-preserving maps on M_2 . *Linear Algebra its Appl*, 2003, 347: 159–187
- 49 King C, Ruskai M B. Minimal entropy of states emerging from noisy quantum channels. *IEEE Trans Inform Theor*, 2001, 47: 192–209
- 50 Liu Z H, Pan W W, Xu X Y, et al. Experimental exchange of grins between quantum Cheshire cats. *Nat Commun*, 2020, 11: 3006
- 51 Guo Y, Taranto P, Liu B H, et al. Experimental demonstration of instrument-specific quantum memory effects and non-Markovian process recovery for common-cause processes. *Phys Rev Lett*, 2021, 126: 230401
- 52 Yu S, Budini A A, Wang Y T, et al. Experimental observation of conditional past-future correlations. *Phys Rev A*, 2019, 100: 050301
- 53 Allen L, Beijersbergen M W, Spreeuw R J C, et al. Orbital angular momentum of light and the transformation of Laguerre-

- Gaussian laser modes. *Phys Rev A*, 1992, 45: 8185–8189
- 54 Berkhout G C G, Lavery M P J, Courtial J, et al. Efficient sorting of orbital angular momentum states of light. *Phys Rev Lett*, 2010, 105: 153601
- 55 Zhang Q, Yu H, Barbiero M, et al. Artificial neural networks enabled by nanophotonics. *Light Sci Appl*, 2019, 8: 42
- 56 Zhou H, Dong J, Cheng J, et al. Photonic matrix multiplication lights up photonic accelerator and beyond. *Light Sci Appl*, 2022, 11: 30
- 57 Liu B H, Li L, Huang Y F, et al. Experimental control of the transition from Markovian to non-Markovian dynamics of open quantum systems. *Nat Phys*, 2011, 7: 931–934
- 58 Breuer H P, Laine E M, Piilo J, et al. Colloquium: non-Markovian dynamics in open quantum systems. *Rev Mod Phys*, 2016, 88: 021002
- 59 Breuer H P, Laine E M, Piilo J. Measure for the degree of non-Markovian behavior of quantum processes in open systems. *Phys Rev Lett*, 2009, 103: 210401
- 60 Lai Y H, Lu Y K, Suh M G, et al. Observation of the exceptional-point-enhanced Sagnac effect. *Nature*, 2019, 576: 65–69
- 61 Feng L, El-Ganainy R, Ge L. Non-Hermitian photonics based on parity-time symmetry. *Nat Photon*, 2017, 11: 752–762
- 62 Miri M A, Alú A. Exceptional points in optics and photonics. *Science*, 2019, 363:
- 63 Xu J S, Sun K, Han Y J, et al. Simulating the exchange of Majorana zero modes with a photonic system. *Nat Commun*, 2016, 7: 13194
- 64 McDonald A, Clerk A A. Exponentially-enhanced quantum sensing with non-Hermitian lattice dynamics. *Nat Commun*, 2020, 11: 5382